

DETC2011-47() %

A STUDY OF GEAR ROOT STRAINS IN A MULTI-STAGE PLANETARY WIND TURBINE GEAR TRAIN USING A THREE DIMENSIONAL FINITE ELEMENT/CONTACT MECHANICS MODEL AND EXPERIMENTS

Phillip E. Prueter

Dynamics and Vibrations Laboratory
Department of Mechanical and
Aerospace Engineering
The Ohio State University
Columbus, OH 43210
prueter.7@buckeyemail.osu.edu

Robert G. Parker*

The Ohio State University
Distinguished Professor Chair
State Key Lab for Mechanical
Systems and Vibration
University of Michigan-Shanghai
Jiao Tong University Joint Institute
Shanghai, China 200240
parker.242@osu.edu

Frank Cunliffe

Managing Director
Orbital2 Ltd.
Warwickshire, UK, CV32 5QL
frankcunliffe@orbital2.com

ABSTRACT

Wind energy has received a great deal of attention in recent years in part due to its minimal environmental impact and improving efficiency. Increasingly complex wind turbine gear train designs, well-known failures in gear train rolling element bearings, and the constant push to manufacture more reliable, longer lasting systems generate the need for more advanced analysis techniques. The objectives of this paper are to examine the mechanical design of an Orbital2 flexible pin multi-stage planetary wind turbine gear train using a three dimensional finite element/contact mechanics model and to compare to full system experiments. Root strain is calculated at multiple locations across the facewidth of ring gears from the computational model and compared to experimental data. Gear misalignment and carrier eccentricity are also considered. Design recommendations for improving load distribution across gear facewidths are also discussed.

1 INTRODUCTION

Analyzing planetary gear systems using computational models presents a unique challenge. Previous work has utilized computational models to examine stresses, strains, and deformations

in planetary gears. One of the first attempts to use a non-linear finite element model to study the behavior of a planetary gear system under static loading was performed by Valco [1]. Kahraman et al. [2] studied the influence of rim thickness of ring gears and compared experimental strain from the roots of ring gear teeth to a two dimensional finite element model. In this comparison, predicted strain shapes matched measured ones closely but the amplitudes differed for certain ring gear thicknesses. It was determined that a two dimensional model can capture ring deflections and hoop stresses while accurate quantification of root strain amplitudes might require a three dimensional model.

Singh et al. [3] examined load sharing in planetary transmissions by comparing root strains from a three dimensional finite element model to experimental results. Strain from the computational model was compared to experiments at multiple circumferential locations on the ring, and the shapes and magnitudes of strain peaks matched well. Root strain, however, was only compared at one location across the facewidth of the ring, making it impossible to detect changes in load distribution due to planet tilting and misalignments. Ligata et al. [4] also used experimental root strain from a ring gear to investigate the influence of manufacturing errors on planetary gear stresses and planet load sharing. Cheon and Parker [5,6] examined the influence of manufacturing errors on dynamic characteristics, load sharing, and criti-

* Address all correspondence to this author.

cal tooth stresses in planetary gears using computational models. James and Harris [7] predicted unequal load sharing in planetary gears due to manufacturing errors using numerical simulations and validated results against experiments.

Several others studies have used finite element models of planetary gears to investigate manufacturing errors, influence of rim thickness, planet load sharing, and even dynamic response. Singh [8] used a three dimensional finite element model of a planetary transmission to study load sharing behavior of planets. Kahraman and Vijayakar [9] examined a two dimensional finite element model of a planetary gear set to determine the effect of internal gear flexibility on deflections and bending stresses. Bodas and Kahraman [10] examined the influence of carrier and gear manufacturing errors on planetary gear sets using a two dimensional finite element model. Parker et al. [11] used a two dimensional finite element model of a planetary gear system to investigate dynamic response. All of these studies used the finite element and contact analysis software program Calyx to model the planetary gear systems investigated. The modeling capabilities of Calyx will be discussed in more detail.

In this paper, root strain from a complete three dimensional finite element/contact mechanics model will be examined and compared to experiments. The load distribution across gear facewidths will be discussed, as will the effects of gravity and relevant manufacturing errors responsible for modulation in strain measured in the experiments.

2 SYSTEM DESCRIPTION

The specific gear train examined in this paper is for a 3.6 MW offshore wind turbine and is designed by Orbital2 Ltd. The complete finite element model of this gear train (Figure 1) is much larger than the ones examined in references [1–11], incorporating multiple planetary stages, a finite element housing, finite element carriers, and flexpins at the planet-carrier connections.

The Orbital2 W3600 gear train contains one fixed-carrier planetary stage (stage 1), one differential planetary stage (stage 2), as well as a stage with a helical wheel and pinion (stage 3). The main rotor shaft that connects to the wind turbine blades attaches to the stage 1 ring via a drive flange and also attaches to the stage 2 carrier. The stage 1 sun connects to the stage 2 ring via a second drive flange. The stage 2 sun connects to the same shaft as the stage 3 wheel that meshes with a helical pinion. The stage 3 helical pinion is attached to the output shaft that powers the generator. The housing has an external reaction arm on either side that is attached to a torque reaction system fixed to the nacelle in actual operation. Details about the finite element model are discussed further in Section 5.

Root strain from the computational model is compared to experimental root strain at eight different strain gauge locations across the facewidths of the two ring gears for stages 1 and 2. The advantage of extracting strain from eight locations across

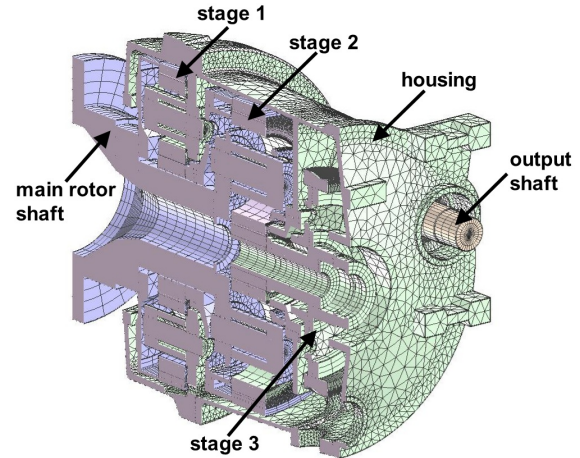


Figure 1. CUTAWAY VIEW OF THE FINITE ELEMENT MODEL OF THE ORBITAL2 W3600 GEAR TRAIN.

the ring facewidth is that it provides information about load distribution across the ring tooth during a planet pass. Experimental root strains from the stage 2 ring, in particular, show an uneven load distribution across the tooth facewidth, with the ring teeth towards the constrained end of the ring being loaded more and teeth towards the free end of the ring being loaded less during a planet pass. Figure 2 shows a cutaway view of the stage 2 ring gear, drive flange, and annulus from the finite element model. This figure depicts the constrained and free ends of the ring, with the constrained end connecting to the stage 2 annulus. The computational model predicts the measured uneven load and confirms that a modified design rectifies this behavior.

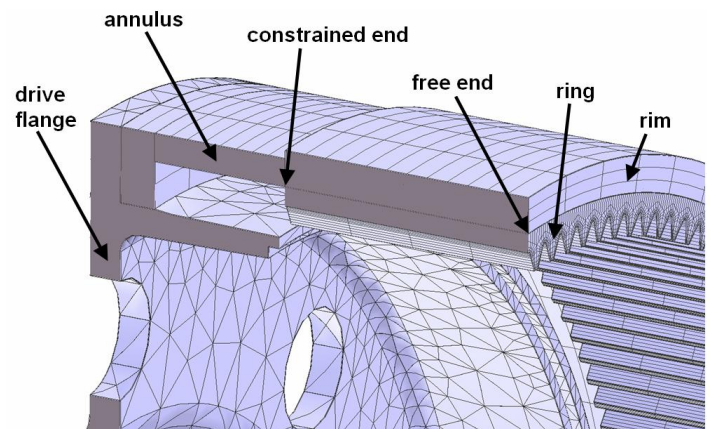


Figure 2. CUTAWAY VIEW OF THE FINITE ELEMENT MODEL OF THE STAGE 2 RING GEAR, DRIVE FLANGE, AND ANNULUS.

3 EXPERIMENTAL STRAIN DATA

As part of their development process, Orbital2 conducted full-scale experiments of the entire gearbox. Orbital2's back-to-back, power circulating experimental test rig as described in [12] is shown in Figure 3. The gearbox housing has external reaction arms on each side that connect to a hydraulic cylinder, as seen just to the right of center at the bottom of Figure 3. This configuration simulates the torque reaction system that connects to these reaction arms when the gearbox is in the wind turbine. The objectives of these experiments were to obtain root strain from the ring gears of both planetary stages to evaluate load distribution, measure sound intensity to evaluate radiated sound power, and record noise and vibration levels at specific locations. The experimental data examined in this paper is ring gear tooth root strain.

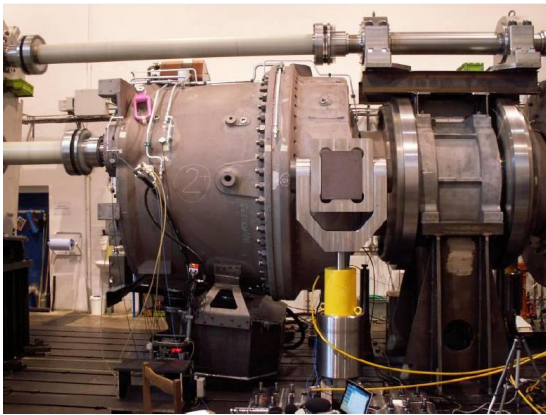


Figure 3. BACK-TO-BACK EXPERIMENTAL TEST RIG CONFIGURATION [12].

There are eight strain gauges across the facewidth of both ring gears. Figure 4 shows the placement of strain gauges in the root of the stage 1 ring gear. The strain gauges were connected to a Bluetooth gear alignment module in quarter bridge configuration. Two independent modules were installed on each annulus. These were separated by approximately 131 degrees on the stage 1 annulus and 180 degrees on the stage 2 annulus. Figure 5 shows the layout of strain gauges across the stage 2 ring facewidth. The position of each strain gauge in the profile and facewidth directions is accurate to within 1 mm. The physical dimensions of each strain gauge are 1.5 mm in the profile direction by 2 mm in the facewidth direction. Strain data was collected during operation of the gearbox under a range of load conditions. In this study, experimental strain data will be correlated to the computational model for the nominal operating input power of 4,114 kW and an output shaft speed of 1,173 rpm.

The strain signal from each gauge exhibits a rounded hump during a planet pass and a sharp peak when a planet contacts the



Figure 4. STRAIN GAUGES PLACED ACROSS THE FACEWIDTH OF THE STAGE 1 RING GEAR [12].

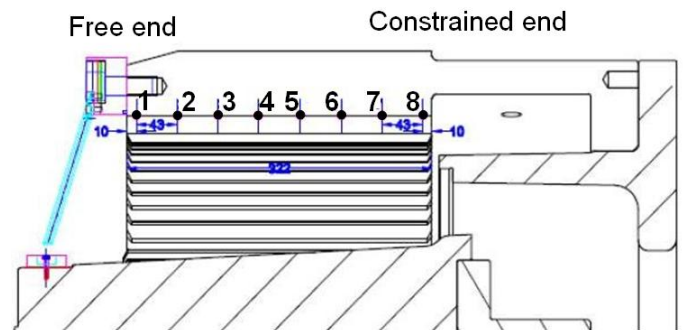


Figure 5. STRAIN GAUGE LAYOUT ACROSS THE STAGE 2 RING FACEWIDTH [12].

instrumented tooth (Figure 6). One of the main points of interest in this paper is to examine strain across the facewidth of the stage 2 ring gear. The experimental strain results show a variation in strain characteristics across the facewidth with more pronounced strain peaks closer to the constrained end of the ring and less pronounced strain peaks near the free end of the ring gear (Figure 6). The design of the system is such that the rings in both stages are constrained at one end where they connect to a drive flange and are unconstrained at the opposite end. Figure 6(a) and 6(b) show the experimental root strain signals from the gauge closest to the free and the constrained ends of the stage 2 ring, respectively. There is a more pronounced strain peak during a planet pass at the constrained end of the ring. In addition to a more distinct peak, there is modulation in the strain signal for the gauge closest to the constrained end. This modulation phenomenon will be investigated further.

Experimental strain data across the facewidth of the stage 1 ring gear will be compared to the finite element/contact mechanics model. While stage 1 experimental strain results show a slight

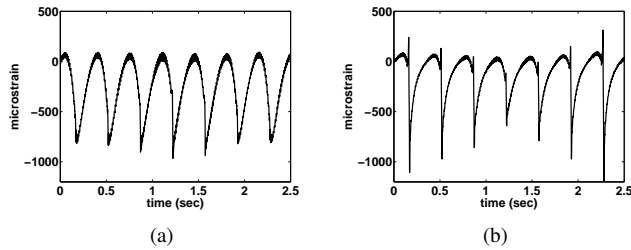


Figure 6. EXPERIMENTAL STRAIN FROM THE GAUGES: (a) CLOSEST TO THE FREE END OF THE STAGE 2 RING, AND (b) CLOSEST TO THE CONSTRAINED END OF THE STAGE 2 RING.

variation in peak-to-peak strain between the free and constrained ends of the ring, there is no distinct strain peak at the constrained end as observed in the stage 2 data. Figure 7(a) shows strain from the gauge closest to the free end of the ring, while Figure 7(b) shows strain from the gauge closest to the constrained end of the ring. The modulation that appeared at the constrained end of the stage 2 ring gear is not present in stage 1.

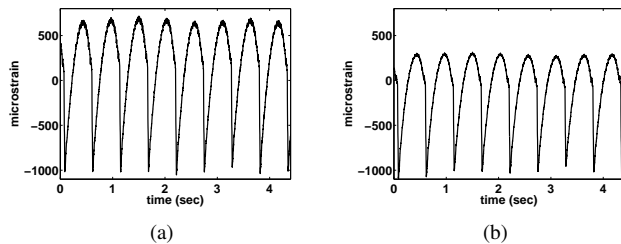


Figure 7. EXPERIMENTAL STRAIN FROM THE GAUGES: (a) CLOSEST TO THE FREE END OF THE STAGE 1 RING, AND (b) CLOSEST TO THE CONSTRAINED END OF THE STAGE 1 RING.

4 FINITE ELEMENT SOFTWARE

Accurately simulating gear tooth contact is complicated. One of the main reasons is that the contact regions on gear teeth are significantly smaller than the other dimensions of the gear bodies. Conventional finite element techniques require highly refined meshes near the contact regions. As the gears move according to their prescribed kinematic motion, the contact location moves along the profile of the tooth. This means that conventional finite element models require a fine mesh over the entire tooth face or the finite element model must be re-meshed for each gear configuration. As discussed in [8], neither of these options present an efficient way to simulate contact in gear systems, especially for planetary configurations with multiple teeth in contact and multiple active meshes. The Calyx finite element/contact mechanics software used in this paper overcomes this obstacle by making the contact model on gear teeth independent of the finite

element model. Figure 8 shows the instantaneous contact pressure on a planet tooth from the finite element model. The contact grid consists of segments in the profile and facewidth directions (partially visible in the discretized contact pattern in Figure 8) that are independent of the finite element mesh. The number of divisions in each direction is a user input in the finite element software.

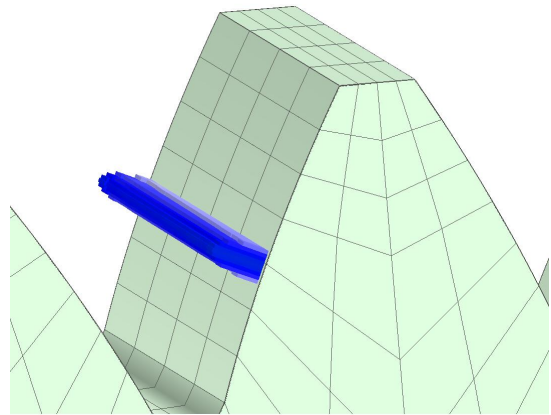


Figure 8. INSTANTANEOUS CONTACT PRESSURE ON A PLANET TOOTH FROM THE FINITE ELEMENT MODEL.

What sets this approach apart from conventional finite element packages is that it uses semi-analytical techniques to compute relative deformations and stresses for points near the contact regions while the finite element model is used to compute deformations and stresses that are outside of the contact regions. The semi-analytical solution is the surface integral form of the Boussinesq solution for a point load on an elastic half-space. The finite element solution and semi-analytical solution are combined by using a matching interface embedded in the contacting body [13]. Load distributions and rigid body movements are calculated using the simplex method that is discussed further in [14]. An overview of the contact analysis and dynamic response comparisons of a finite element/contact mechanics model of a spur gear pair to experiments are discussed in [15].

5 FINITE ELEMENT MODEL

5.1 Model Details

The complex yet efficient design of the Orbital2 W3600 gear train showcases the sophisticated modeling capabilities used herein. A cutaway view of the full finite element model is shown in Figure 1; more detailed views of both planetary stages are in Figure 9. The three dimensional finite element model of the Orbital2 W3600 gear train includes a finite element housing, finite element carriers, drive flanges, and flexible pins, also known as

the Hick's flexpin [16], in both of the planetary stages. The carriers, flexpins, shafts, and gears are given the material properties of steel and the housing, drive flanges, and stage 2 support plate are given the material properties of cast iron. Tooth geometry features, including tip modifications and root fillet radii, are accurately modeled. Bearings connecting the flexpins to the planets and shafts to the housing are modeled using stiffness matrices.

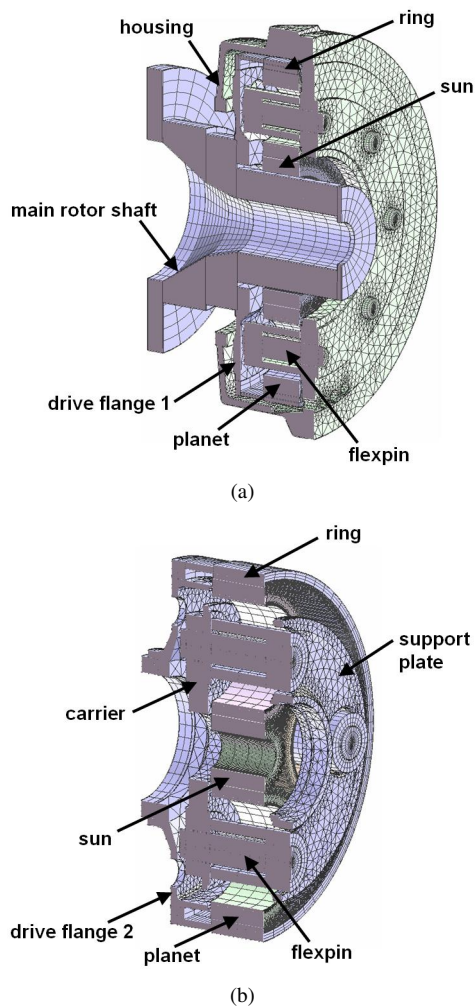


Figure 9. CUTAWAY VIEW OF THE FINITE ELEMENT MODEL OF: (a) STAGE 1, AND (b) STAGE 2.

The finite element model boundary conditions are shown in Figure 10. The model is supported at the front of the main rotor shaft. The reaction arms on either side of the housing are constrained in the rotational degree of freedom with respect to the main axis of the gear box as shown. These constraints simulate the boundary conditions of the experimental test rig. Gravity is included in the model; it plays a key role in the overall model deflection and the modulation observed in the stage 2 strain signals.

It was determined from simulations of a simpler model that the finite element housing and finite element carriers are necessary to capture all of the effects of gravity. The effects of gravity on model deflections and strain modulation will be discussed further in Section 7.

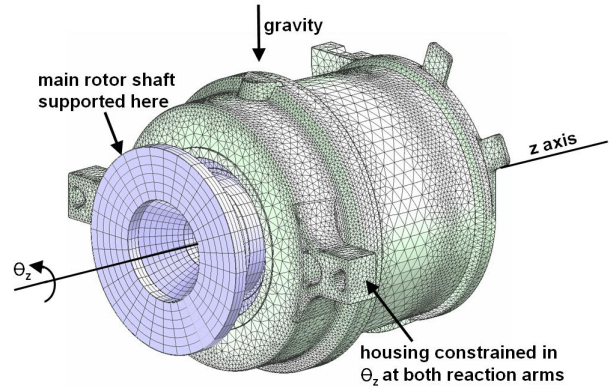


Figure 10. BOUNDARY CONDITIONS ON THE FINITE ELEMENT/CONTACT MECHANICS MODEL.

5.2 Flexpins

One of the main design goals in epicyclic gear systems is to ensure equal load sharing between planets. Torsional wind-up of the carrier, machining tolerances, position accuracy of the pin, and bearing clearances all reduce effective load sharing and cause misaligned contact patterns in planetary gears. Epicyclic gear systems are often equipped with straddle-mounted planets having pins supported on the input and output sides of the carrier [17]. This type of straddle-mounted pin cannot tilt under a planet load and leads to a heavy and complex carrier. Many different designs have been employed to achieve load sharing between planets. This includes introducing more elastic compliance into the system using flexible ring gears. Other designs have implemented floating ring gears, sun gears, and planet carriers. An especially successful way to achieve load sharing among planets and evenly distribute tooth contact patterns is the flexible pin, also called flexpin, that was invented in 1964 by Ray J. Hicks [16]. This novel method of providing load sharing between planets has been applied to a large variety of industrial aerospace, marine, and wind turbine gear trains [18].

The flexpin employs a double cantilevered pin design shown in Figure 11. Not only does it eliminate the need for straddle mounting, but it allows use of the maximum number of planets subject to tip-to-tip clearance constraints. An important design feature is that the pin that is cantilevered at one end to the carrier and the spindle that is cantilevered to the other end of the pin are co-axial, which enables deflection in two planes. This feature

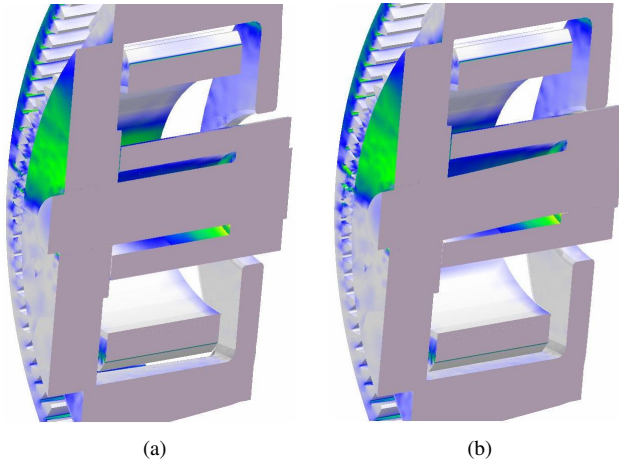


Figure 11. (a) CUTAWAY VIEW OF UNDERFORMED STAGE 2 FLEXPIN (b) CUTAWAY VIEW OF LOADED STAGE 2 FLEXPIN WITH EXAGGERATED DEFORMATION.

makes the flexpin virtually self aligning [19]. Essentially, the flexpin can deflect independently in a circumferential direction, which helps equalize force distribution among planets. When tooth mesh forces are applied to a planet supported by a flexpin, the angular deflection caused by bending of the pin cantilevered to the carrier can be offset by the angular deflection in the opposite direction caused by the bending of the spindle cantilevered to the opposite end of the pin [17]. This prevents tilting of the planet (Figure 11(b)). In a recent study, Montestruc [20] noted that the Hicks flexpin design improves planet load sharing and power to weight ratios in planetary transmissions. The finite element software used herein accurately models flexpins for both planetary stages. Figure 11(a) shows a cutaway view of the finite element model of an undeformed stage 2 flexpin. Figure 11(b) shows a cutaway view of the same flexpin with exaggerated deformation under nominal loading. The flexpin is behaving as expected, with the spindle remaining level and most of the deflection occurring in the pin cantilevered to the carrier.

6 COMPUTATIONAL STRAIN DATA

6.1 Strain Data Extraction

When dealing with a large, three dimensional finite element model, computational efficiency is a concern. While Calyx can efficiently solve contact problems, the sheer size of the gear train model and the number of active meshes make simulations computationally intensive. A true strain time history for a ring tooth on a planetary stage would require running that stage for many mesh cycles in order to obtain root strain readings for multiple planet passes. This is not practical for a large, three dimensional model. In this study, this obstacle is overcome by running each planetary stage statically for one mesh cycle divided into 20 time steps. This was determined to be a sufficient number of time

steps after comparing it to simulations with twice as many steps per mesh cycle that yielded very little change in peak-to-peak strain. By extracting strain from the root of each tooth the entire way around the ring gear a strain signal is reconstructed that shows a strain peak for each strain gauge at each planet location. The result is a strain signal at each gauge location across the facewidth corresponding to a planet pass at each planet location. For instance, the stage 2 strain peaks correspond to a planet pass at the locations of the four different planets shown in Figure 12(a). Figure 12(b) shows the corresponding strain peaks for each planet location; of the eight gauges, the gauge closest to the free end of the stage 2 ring gear is shown. This process allows a sufficient number of contact parameters to be used without sacrificing computational efficiency.

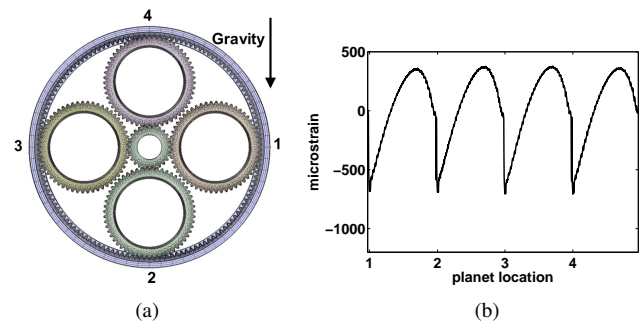


Figure 12. (a) STAGE 2 PLANET LOCATIONS (b) STRAIN PEAKS FROM THE FREE END OF THE RING THAT CORRESPOND TO PLANET LOCATIONS SHOWN IN (a).

Strain from the stage 1 ring is extracted in a similar manner. A simulation is run that corresponds to one mesh cycle for the stage 1 planetary set, and the strain signal at each gauge location is reconstructed as described for stage 2. Figure 13(a) depicts the planet locations, and Figure 13(b) shows the corresponding strain peaks for each planet pass for the gauge closest to the free end of the ring.

Sufficient mesh refinement is required on the ring teeth to accurately calculate root strains. The contact grid must also contain sufficient divisions in the facewidth direction. Using the appropriate contact parameters such as number of face divisions is especially important in this study because variation in strain characteristics across the facewidth is examined. Gravity also becomes important when looking at the strain modulation seen in the stage 2 experimental data.

6.2 Strain Sensitivity

Strain sensitivity to gauge location is examined due to its importance when it comes to matching experiments. The strain gauges are 1.5 mm in the profile direction by 2 mm in the facewidth direction and placed in the bottom of the root. Strain

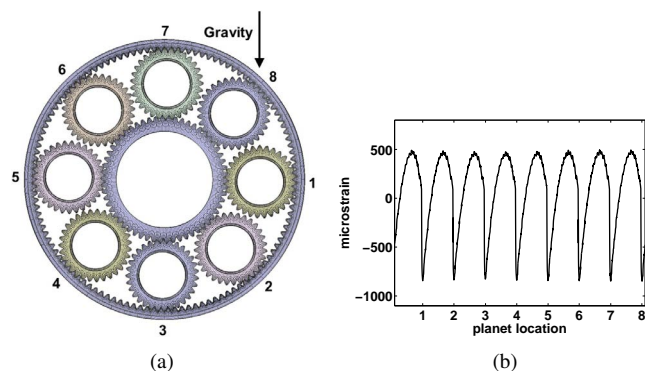


Figure 13. (a) STAGE 1 PLANET LOCATIONS (b) STRAIN PEAKS FROM THE FREE END OF THE RING THAT CORRESPOND TO PLANET LOCATIONS SHOWN IN (a).

gauge position is accurate to within 1 mm in both the profile and facewidth directions. Because the strain gauges physically cover a region in the root, strain from the finite element model is averaged over three locations in the profile direction for each gauge. One point corresponds to the center of the strain gauge, and the two other points correspond to either end of the gauge, that is, 3/4 mm each way in the profile direction. Looking at strain from each of these points separately illustrates that strain is highly sensitive to gauge position in the profile direction. Figure 14(a) shows the three locations in the root of the stage 2 ring where strain is averaged. Gauge location A is 3/4 mm in the profile direction from location B, and gauge location C is 3/4 mm from location B in the opposite direction. Figures 14(b), 14(c), and 14(d) show the strain peaks for each planet location as described above at gauge locations A, B, and C, respectively.

Figure 14 illustrates the significance of the location of the gauge in the root. A gauge that is positioned 3/4 mm either way in the profile direction, still within the tolerance of gauge position, can yield strain curves that are shifted more towards tension or compression. This is an important point when correlating the computational strain results to experiments.

6.3 Correlation to Experiments

When comparing the strain data from the finite element model (Figures 15 and 16) to the experiments (Figures 6 and 7), the shape of the strain peaks matches well. The experimental strain time history can not be directly compared to experiments because the finite element model was run for one mesh cycle for each planetary stage. Data from each ring tooth was pieced together to generate a strain signal that shows planet passes that correspond to the planet locations shown in Figures 13 and 12 for stages 1 and 2 respectively. Moreover, the shapes and amplitudes of strain peaks that correspond to each planet location are analogous to experimental strain peaks at the same planet locations. The computational strain signal does not resemble the experiments in number of planet passes because strain is not extracted

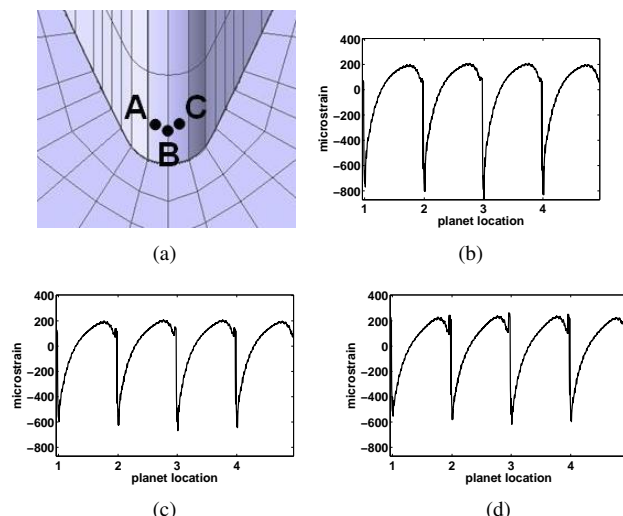


Figure 14. (a) LOCATIONS IN THE ROOT OF THE STAGE 2 RING WHERE STRAIN IS EXTRACTED (b) STRAIN FROM GAUGE LOCATION A (c) STRAIN FROM GAUGE LOCATION B (d) STRAIN FROM GAUGE LOCATION C.

from one instrumented tooth in real time as in the experiments. In order to validate the use of a script to reconstruct root strain and to relate ring tooth location to peak-to-peak root strain, strain was extracted from one stage 2 ring tooth from the finite element model for simulations run over a complete ring revolution. Strain modulation due to gravity and eccentricity is observed in these simulations and will be discussed further in Section 7.

The stage 1 computational strain data matches the experiments well in that it lacks modulation in the strain signal and the peak-to-peak strains are comparable. Even though some of the strain peaks seem shifted toward either tension or compression, this could be due to strain gauge position error in the root of the tooth, as discussed above. Figure 15(a) shows strain extracted from the Calyx model at the gauge location closest to the free end of the stage 1 ring, and Figure 15(b) shows strain from the gauge location closest to the constrained end of the stage 1 ring. These computational strain peaks indicate that the finite element model is behaving similarly to the gearbox used to obtain experimental root strain, and in particular, the variation in strain characteristics across the facewidth of the stage 1 ring is captured. These strain peaks correspond to the planet locations in Figure 13.

When comparing stage 2 strain data to experiments, it is clear that during a planet pass a sharp spike in strain and rapid reversal from tension to compression occur in both the experimental and computational strain near the constrained end of the ring. This spike is not present near the free end of the ring where the rapid strain reversal due to mesh contact is exceeded by a slower transient related to each passing planet. Figure 16(a) shows strain from the finite element model at the gauge location closest to the free end of the stage 2 ring, and Figure 16(b) shows strain from the gauge location closest to the constrained end of the stage 2

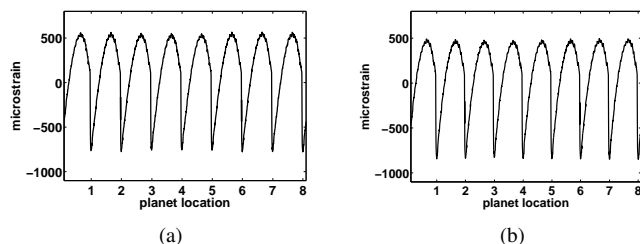


Figure 15. (a) STRAIN FROM THE GAUGE CLOSEST TO THE FREE END OF THE STAGE 1 RING (b) STRAIN FROM THE GAUGE CLOSEST TO THE CONSTRAINED END OF THE STAGE 1 RING.

ring. These strain peaks correspond to the planet locations depicted in Figure 12. This variation in strain characteristics across the gear facewidth is mainly attributed to the local deflection of the stage 2 ring and annulus (Figure 2). During a planet pass, the free end of the ring deflects more than the constrained end causing an uneven load distribution. This is expected because of the added stiffness at the constrained end of the ring where the rim connects to the annulus and drive flange (Figure 2).

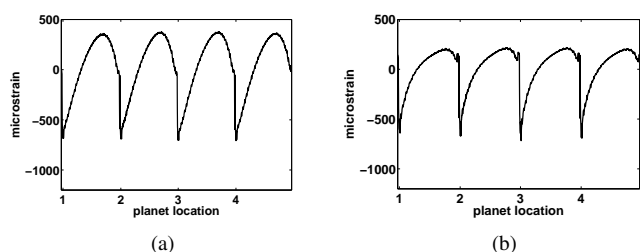


Figure 16. (a) STRAIN FROM THE GAUGE CLOSEST TO THE FREE END OF THE STAGE 2 RING (b) STRAIN FROM THE GAUGE CLOSEST TO THE CONSTRAINED END OF THE STAGE 2 RING.

7 STRAIN MODULATION

7.1 Effects of Gravity and Model Deflections

Even though the finite element model is capturing the uneven load distribution across the facewidth of the stage 2 ring gear, it does not capture the modulation in strain observed over a ring revolution near the constrained end of the ring in the experiments as seen in Figure 6(b). While a slight modulation exists in the computational strain, it is much less than the modulation in experimental strain. One contributing factor to this modulation is gravity. Because the gearbox is supported at the front as seen in Figure 10, gravity causes the back end to sag under its own weight. This causes the stage 2 ring and annulus to sag as well. The weight of the ring and annulus adds to the ring-planet mesh force at planet location 3 and subtracts from the ring-planet mesh force at planet location 1. The largest strain peak corresponds

to planet location 3 as described in Figure 12, and the smallest strain peak occurs at planet location 1. It is for this reason that including gravity in the model is essential.

It is not known what planet pass location corresponds to the minimum and maximum experimental strain peaks for the strain gauge closest to the constrained end of the stage 2 ring. It is reasonable to assume that the maximum occurs at planet location 3 and the minimum occurs at planet location 1, as shown in Figure 12. The location of the planets with respect to gravity is important when trying to understand the modulation. Simulations with and without eccentricity run over a ring revolution will be discussed in Section 7.2 and provide insight into the relationship between the instrumented ring tooth location and peak-to-peak strain. The contribution of gravity and eccentricity to strain modulation will be investigated.

Figure 17(a) shows a cutaway view of the stage 1 sun-stage 2 ring subassembly, and Figure 17(b) shows the same view with exaggerated deformation. The horizontal lines represent the central axis of the undeformed gearbox. The stage 2 ring and annulus deflect in the direction of gravity. The stage 2 carrier and planets do not deflect as much in the direction of gravity because the stage 2 carrier is connected to the main rotor shaft that is supported at the front of the gearbox as shown in Figure 10. This is significant because it supports the idea that the deflection of the ring increases the strain peak at planet location 3 and decreases the strain peak at planet location 1.

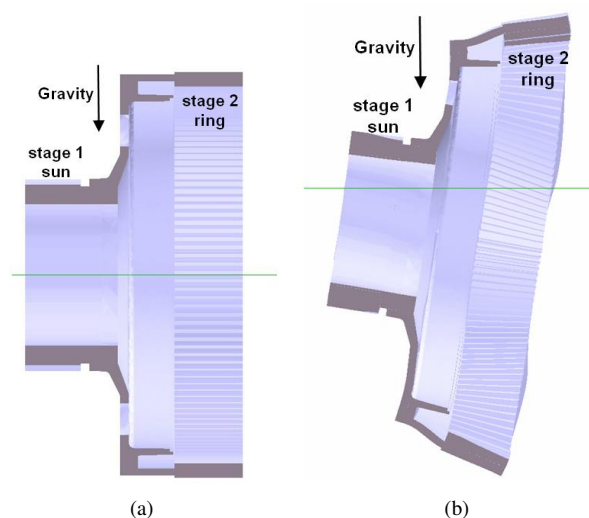


Figure 17. CUTAWAY VIEW OF THE STAGE 1 SUN-STAGE 2 RING SUBASSEMBLY: (a) UNDEFORMED, AND (b) WITH EXAGGERATED DEFORMATION.

Figure 18 explains this further by showing the instantaneous contact patterns at the ring-planet meshes at planet locations 1 and 3. At planet location 1, when the ring deflects in the direction

of gravity, it essentially decreases the load at the ring-planet mesh because contact is on the top of the ring tooth (contact force is primarily downward on the ring tooth). On the contrary, at planet location 3, the ring deflection in the direction of gravity increases the load at the ring-planet mesh because the contact is on the bottom of the ring tooth (contact force is primarily upward on the ring tooth). Thus, the maximum experimental peak-to-peak strain during a planet pass likely occurs near planet location 3, and the minimum peak-to-peak strain during a planet pass likely occurs near planet location 1. The instantaneous contact patterns shown in Figures 18(a) and 18(b) also illustrate that the stage 2 ring teeth are loaded more towards the constrained end. This is also reflected in the computational strain from each end of the ring during a planet pass as shown in Figure 16.

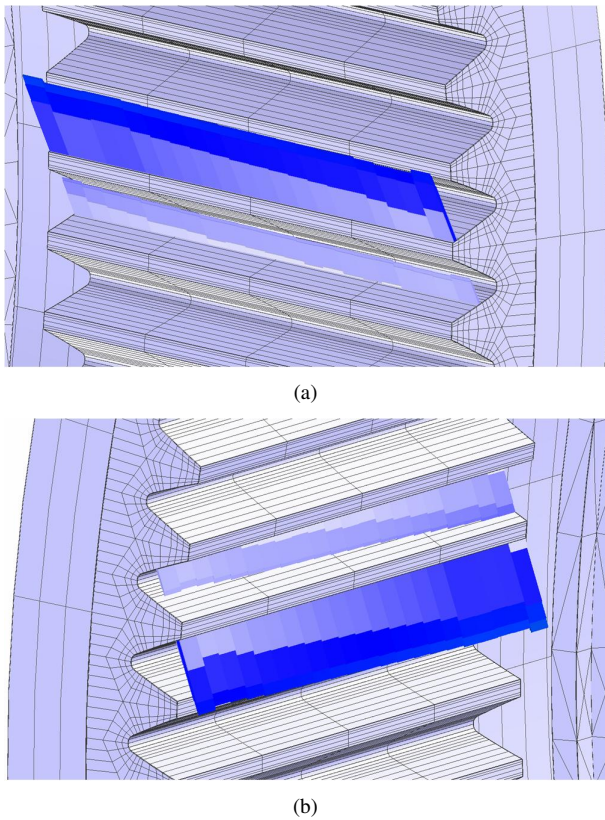


Figure 18. (a) INSTANTANEOUS CONTACT FORCES ON STAGE 2 RING AT PLANET LOCATION 1 (b) INSTANTANEOUS CONTACT FORCES ON STAGE 2 RING AT PLANET LOCATION 3.

Examining tangential bearing reaction forces of the stage 2 planets further indicates that gravity contributes to the modulation in strain and influences planet load sharing. Figure 19(a) shows the tangential bearing reaction forces of the stage 2 planets for the model without gravity, and Figure 19(b) shows the reaction forces for the model with gravity included. For the model

without gravity, there is little difference in planet bearing reaction forces. For the model with gravity included, the planet at location 1 yields the lowest bearing reaction force, and the planet at location 3 yields the highest bearing reaction force. These bearing reaction forces are consistent with the minimum and maximum root strain peaks that occur near the constrained end of the stage 2 ring during a planet pass at these planet locations. The model without gravity exhibits no modulation in strain at any gauge location across the ring facewidth.

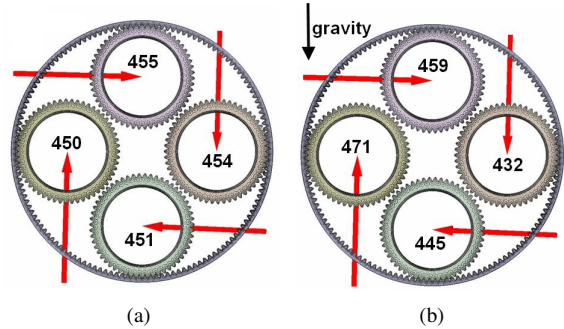


Figure 19. TANGENTIAL BEARING REACTION FORCES (kN) OF THE STAGE 2 PLANETS FOR: (a) THE MODEL WITHOUT GRAVITY, AND (b) THE MODEL WITH GRAVITY.

7.2 Carrier Eccentricity

Even though gravity contributes to the strain modulation, there is still some contributing factor that is not being captured by the computational model because the modulation from the finite element model is not as drastic as the experimental strain at the constrained end of the stage 2 ring. For this reason, stage 2 carrier eccentricity is considered. Eccentricity is simulated by applying unloaded bearing deformation to the two bearings connecting the main rotor shaft and stage 2 support plate to the housing (connector locations shown in Figure 20). A value and direction of unloaded deformation are defined for the race attached to the main rotor shaft/support plate relative to the housing, in the housing reference frame. Because the stage 2 carrier is attached to the main rotor shaft and support plate, this simulates carrier eccentricity in the defined direction.

Different values of carrier eccentricity are investigated in the direction opposite gravity. It was determined that as carrier eccentricity in this direction increases, the modulation in strain near the constrained end of the stage 2 ring becomes more significant. Eccentricities of 100, 200, 400, 500, and 1000 μm are investigated. These are reasonable values given the large size of the gearbox. For example, the outside diameter of the stage 2 ring is 1.93 meters. Figures 21(a) and 21(b) show computational strain from the free and constrained end of the stage 2 ring, respectively, with 200 μm carrier eccentricity in the direction opposite

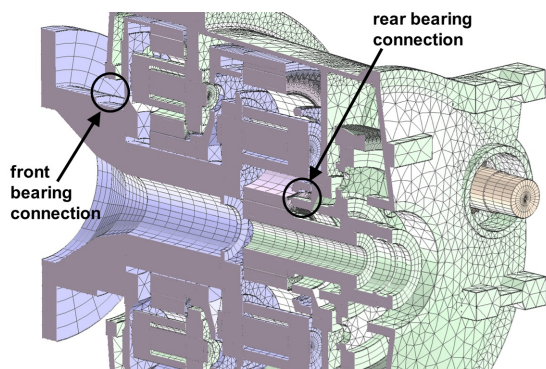


Figure 20. TWO BEARING CONNECTIONS GIVEN UNLOADED DEFORMATION TO SIMULATE ECCENTRICITY THAT CONNECT THE MAIN ROTOR SHAFT AND THE STAGE 2 CARRIER/SUPPORT PLATE TO THE HOUSING.

gravity. Similarly, Figures 21(c) and 21(d) show strain from the same locations but with 500 μm carrier eccentricity in the same direction.

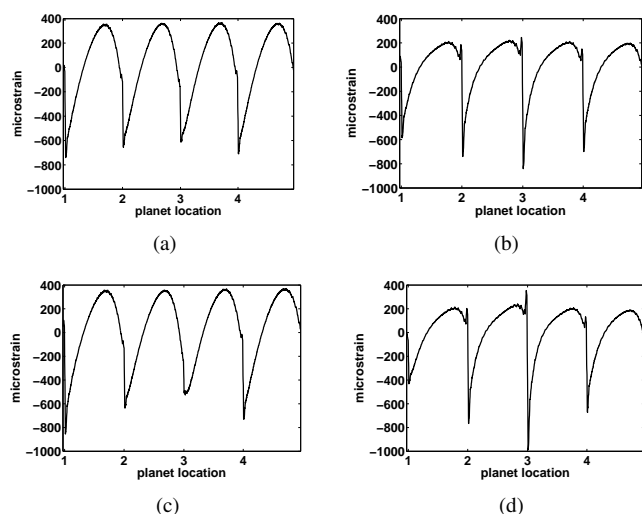


Figure 21. (a) STRAIN FROM FREE END OF STAGE 2 RING GEAR WITH 200 μm CARRIER ECCENTRICITY (b) STRAIN FROM CONSTRAINED END OF STAGE 2 RING GEAR WITH 200 μm CARRIER ECCENTRICITY (c) STRAIN FROM FREE END OF STAGE 2 RING GEAR WITH 500 μm CARRIER ECCENTRICITY (d) STRAIN FROM CONSTRAINED END OF STAGE 2 RING GEAR WITH 500 μm CARRIER ECCENTRICITY.

Figure 21 shows that introducing carrier eccentricity in the finite element model in the direction opposite gravity indeed enhances the strain modulation at the constrained end of the stage 2 ring. The minimum peak-to-peak strain occurs during a planet

pass at planet location 1, and the maximum peak-to-peak strain occurs during a planet pass at planet location 3. The modulation increases with carrier eccentricity. Furthermore, the planet location that yields the minimum peak-to-peak strain during a planet pass at the constrained end of the ring corresponds to the planet location that yields a maximum peak-to-peak strain during a planet pass at the free end of the ring and vice versa. This is consistent with the experimental strain data shown in Figure 6. For instance, during a planet pass, planet location 1 yields the minimum peak-to-peak strain at the constrained end and the maximum peak-to-peak strain at the free end. Planet location 3 yields the maximum peak-to-peak strain at the constrained end and minimum peak-to-peak strain at the free end.

Tangential bearing reaction forces of the stage 2 planets from the finite element model with carrier eccentricity are consistent with the strain modulation that occurs near the constrained end of the ring. Figures 22(a) and 22(b) show stage 2 tangential bearing reaction forces for the model with 200 μm and 500 μm carrier eccentricity in the direction opposite gravity respectively. It can be seen that as eccentricity increases, the difference between the minimum and maximum bearing reaction forces at planet locations 1 and 3 also increases. These results are consistent with root strain behavior. The larger the difference in the planet bearing reaction forces at locations 1 and 3, the larger the difference in peak-to-peak strain during a planet pass at locations 1 and 3 near the constrained end of the ring.

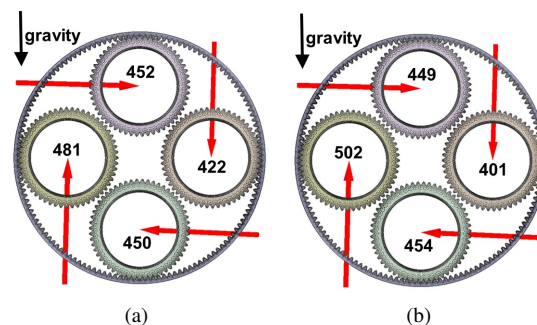


Figure 22. TANGENTIAL BEARING REACTION FORCES (kN) OF THE STAGE 2 PLANETS FOR: (a) THE MODEL WITH 200 μm ECCENTRICITY, AND (b) THE MODEL WITH 500 μm ECCENTRICITY.

In order to relate carrier eccentricity in the direction opposite to gravity and strain modulation at the constrained end of the ring, eccentricity versus the difference in maximum and minimum peak-to-peak strain during a planet pass is plotted in Figure 23. As seen in Figure 23, carrier eccentricity definitely contributes to modulation.

In order to better understand the strain modulation observed in both the experiments and the finite element model and to verify the use of a script to extract root strain, two simulations were

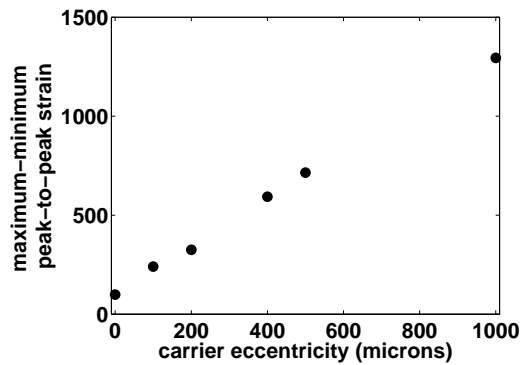


Figure 23. STAGE 2 CARRIER ECCENTRICITY IN THE DIRECTION OPPOSITE GRAVITY VS. MAXIMUM-MINIMUM PEAK TO PEAK STRAIN DURING A PLANET PASS FROM THE FINITE ELEMENT MODEL.

run over a stage 2 ring revolution (one with no eccentricity and one with 500 μm eccentricity in the direction opposite gravity). In the interest of computational efficiency, 20 time steps were used in between each planet pass. Strain was extracted from one ring tooth to replicate the instrumented tooth in the experimental setup. Even this relatively low number of time steps over a ring revolution illustrates the modulation in strain near the constrained end of the stage 2 ring for both cases. Figures 24(a) and 24(b) show the computational root strain from the constrained end of the stage 2 ring over a ring revolution with no eccentricity and 500 μm eccentricity in the direction opposite gravity respectively. The peaks corresponding to planet locations 1 and 3 (as shown in Figure 12(a)) are labeled. These figures support the idea that gravity contributes to strain modulation and that carrier eccentricity enhances it. These simulations verify that the minimum and maximum strain peaks occur near planet locations 1 and 3 respectively and confirm that the finite element model is capturing strain modulation similar to what was observed in the experiments. As seen in the experiments, the modulation repeats every six planet passes which corresponds to the number of planets that mesh with the instrumented ring tooth over a ring revolution.

8 EXAMINING A MORE FLEXIBLE STAGE 2 ANNULUS

With the computational model validated against experiments, the design of certain components can be changed to understand how the change affects the mechanics. One design change that is examined applies to the stage 2 annulus. As was discussed earlier, the uneven loading of the stage 2 ring during a planet pass results from the local deformation of the stage 2 ring. A proposed design adds holes around the annulus with the thought being that a more compliant annulus would yield better load distribution across the ring facewidth. This added compli-

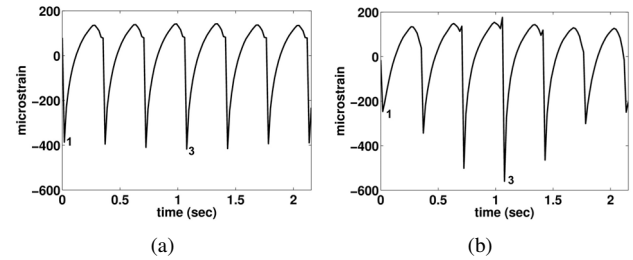


Figure 24. ROOT STRAIN FROM THE CONSTRAINED END OF THE STAGE 2 RING OVER A RING REVOLUTION FROM THE FINITE ELEMENT MODEL WITH: (a) NO ECCENTRICITY, AND (b) 500 μm ECCENTRICITY.

ance would cause the ring to deflect more evenly in the radial direction during a planet pass. A smooth distribution of material is also added to the rim of the ring gear such that the radial thickness at the free end is greater than at the constrained end. Figure 25(a) shows the finite element model of the stage 2 ring and annulus as tested, while Figure 25(b) shows the new design.

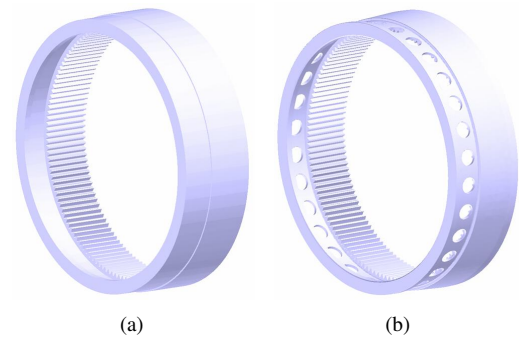


Figure 25. (a) FINITE ELEMENT MODEL OF THE STAGE 2 RING AND ANNULUS AS TESTED (b) FINITE ELEMENT MODEL OF THE PROPOSED DESIGN OF THE MORE FLEXIBLE STAGE 2 ANNULUS.

When results from this proposed design for the stage 2 annulus are compared to the original model, a noticeable improvement in strain characteristics across the stage 2 ring gear occurs. Specifically, the sharp spike in strain that was observed near the constrained end of the ring during a planet pass for the original design is not present. Figures 26(a) and 26(b) show computational strain from the finite element model with the more flexible annulus at the free and constrained end of the stage 2 ring, respectively. The reason that the sharp spike in strain during a planet pass is not present in the model with the more flexible annulus is due to the local deflection of the stage 2 ring. The more compliant annulus deflects more uniformly in the radial direction.

Figure 27 further illustrates this by comparing ring rim deflections for both designs. Clearly, the more flexible annulus

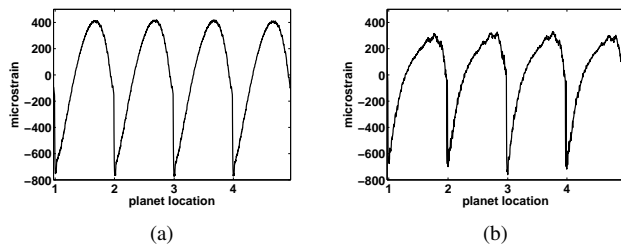


Figure 26. COMPUTATIONAL STRAIN FROM THE MODEL WITH THE MORE FLEXIBLE STAGE 2 ANNULUS FROM: (a) THE GAUGE LOCATION CLOSEST TO THE FREE END OF THE STAGE 2 RING, AND (b) THE GAUGE LOCATION CLOSEST TO THE CONSTRAINED END OF THE STAGE 2 RING.

yields a more uniform ring deflection in the radial direction whereas the ring for the original design deflects more in the radial direction at the free end than at the constrained end. This deflection causes the constrained end of the ring to be loaded more for the original design, thus causing the sharp strain peak during a planet pass. The stage 2 annulus with holes around the circumference effectively improves load distribution across the facewidth of the stage 2 ring.

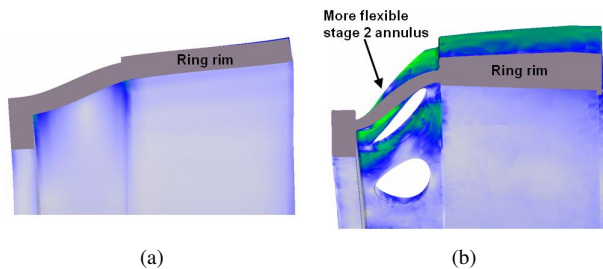


Figure 27. (a) DEFORMATION OF THE ORIGINAL STAGE 2 RING RIM AND ANNULUS (b) DEFORMATION OF THE PROPOSED DESIGN OF THE STAGE 2 RING RIM WITH MORE FLEXIBLE ANNULUS.

9 CONCLUSIONS

In this paper, a complete finite element/contact mechanics model of the Orbital2 W3600 wind turbine gear train was constructed. This model includes a finite element housing, finite element carriers and drive flanges, finite element models of flexpins implemented in both planetary stages, and accurate modeling of the contacting gear teeth using a multi-body contact solver. Root strain from the rings of both planetary stages was compared to experiments, and in general there was good agreement. It was determined that uneven loading of the stage 2 ring teeth during a planet pass was due mainly to local deformation of the ring into a conical shape because of differing constraints on the two

sides of the teeth. It was also determined that gravity and, very likely, carrier eccentricity contribute to the modulation in strain observed over a ring revolution at the constrained end of the stage 2 ring. Adding carrier eccentricity to the finite element/contact mechanics model in the direction opposite gravity enhances this modulation and yields better correlation to stage 2 experimental strain. Calyx has the capability to investigate design changes of different components such as the stage 2 annulus. Looking at different designs of components leads to a better understanding of how the gear train deforms under load and provides insight into how to improve load distribution across the ring facewidths. A more compliant design for the stage 2 annulus was investigated. This design successfully reduces variation in strain characteristics across the facewidth of the ring because the annulus bends more than the original design when a planet tooth meshes with a ring tooth. Computational models, such as the one used in this paper, are extremely valuable design tools when attempting to understand and improve complex gear train designs such as the Orbital2 W3600.

ACKNOWLEDGMENTS

The authors would like to thank Orbital2 Ltd. for funding this work and for giving permission to publish the experimental and computational data. The authors would also like to thank Mr. Vilem Rosko and Mr. Remko Gerbenzon of Orbital2 Ltd. for providing all of the necessary parameters and for their guidance and assistance in modeling the gear train. Transmission Dynamics Ltd. is also acknowledged for contributions on experimental strain data. Furthermore, the authors would like to thank Dr. Sandeep Vijayakar of Advanced Numerical Solutions for granting access to Transmission3D and Calyx software and for providing insight into finite element modeling and root strain extraction from the computational model.

REFERENCES

- [1] Valco, M., 1992. "Planetary gear train ring gear and support structure investigation". PhD thesis, Cleveland State University.
- [2] Kahraman, A., Ligata, H., and Singh, A., 2010. "Influence of ring gear rim thickness on planetary gear set behavior". *Journal of Mechanical Design*, **132**, Feb., pp. 021002–1–021002–8.
- [3] Singh, A., Kahraman, A., and Ligata, H., 2007. "Internal gear strains and load sharing in planetary transmissions - model and experiments". In ASME Design Engineering Technical Conferences. DETC2007-35047.
- [4] Ligata, H., Kahraman, A., and Singh, A., 2008. "An experimental study of the influence of manufacturing errors on the planetary gear stresses and planet load sharing". *Journal of Mechanical Design*, **130**, Apr., pp. 041701–1–041701–9.
- [5] Cheon, G.-J., and Parker, R., 2004. "Influence of manu-

- facturing errors on the dynamic characteristics of planetary gear systems”. *The Korean Society of Mechanical Engineers International Journal*, **18**(4), pp. 606–621.
- [6] Cheon, G.-J., and Parker, R., 2004. “Influence of bearing stiffness on the static properties of a planetary gear system with manufacturing errors”. *The Korean Society of Mechanical Engineers International Journal*, **18**(11), pp. 1978–1988.
- [7] James, B., and Harris, O., 2002. “Predicting unequal planetary load sharing due to manufacturing errors and system deflections, with validation against experiments”. In SAE Transmission and Driveline Systems Symposium. 2002-01-0699.
- [8] Singh, A., 2005. “Application of a system level model to study the planetary load sharing behavior”. *Journal of Mechanical Design*, **127**, May, pp. 469–476.
- [9] Kahraman, A., and Vijayakar, S. M., 2001. “Effect of internal gear flexibility on the quasi-static behavior of a planetary gear set”. *Journal of Mechanical Design*, **123**(3), Sept., pp. 408–415.
- [10] Bodas, A., and Kahraman, A., 2004. “Influence of carrier and gear manufacturing errors on the static load sharing behavior of planetary gear sets”. *The Japan Society of Mechanical Engineers International Journal*, **47**(3), pp. 908–915.
- [11] Parker, R., Agashe, V., and Vijayakar, S., 2000. “Dynamic response of a planetary gear system using a finite element/contact mechanics model”. *Journal of Mechanical Design*, **122**(3), Sept., pp. 304–310.
- [12] Smurthwaite, D., and Rosinski, J., 2010. Orbital2 S3600 Planet Gear Load Sharing. Transmission Dynamics Technical Report No. TD-10-2130-01.
- [13] Vijayakar, S., 1991. “A combined surface integral and finite-element solution for a three-dimensional contact problem”. *International Journal for Numerical Methods in Engineering*, **31**(3), Mar., pp. 525–545.
- [14] Vijayakar, S., Busby, H., and Houser, D., 1988. “Linearization of multibody frictional contact problems”. *Computers and Structures*, **29**(4), pp. 569–576.
- [15] Parker, R., Vijayakar, S., and Imajo, T., 2000. “Non-linear dynamic response of a spur gear pair: Modelling and experimental comparisons”. *Journal of Sound and Vibration*, **237**(3), Oct., pp. 435–455.
- [16] Hicks, R., 1967. Load Equalizing Means for Planetary Pinions. U.S. Patent No. 3,303,713.
- [17] Fox, G., and Jallet, E. Use of the Integrated Flexpin Bearing for Improving the Performance of Epicyclical Gear Systems. Technical Paper by the Timken Company.
- [18] Hicks, R., Cunliffe, F., and Giger, U., 2004. Optimised Gearbox Design For Modern Wind Turbines. Technical Paper by Orbital2 Ltd.
- [19] Hicks, R., 1969-70. “Experience with compact orbital gears in service”. *Proc Instn Mech Engrs*, **184 Pt 30**.
- [20] Montestruc, A., 2011. “Influence of planet pin stiffness on load sharing in planetary gear drives”. *Journal of Mechanical Design*, **133**, Jan., pp. 014501–1–014501–7.